

**FORCHHEIMER LAW IN COMPUTATIONAL  
AND EXPERIMENTAL STUDIES OF FLOW  
THROUGH POROUS MEDIA AT PORESCALE  
AND MESOSCALE**

MAŁGORZATA PESZYŃSKA

Department of Mathematics, Oregon State University  
Corvallis, OR, 97331, USA  
E-mail: mpsz@math.oregonstate.edu

ANNA TRYKOZKO

Interdisciplinary Centre for Mathematical and Computational Modelling, University of Warsaw  
ul. Pawińskiego 5a, 02-106 Warsaw, Poland  
E-mail: a.trykozko@icm.edu.pl

and

WOJCIECH SOBIESKI

Faculty of Technical Sciences, University of Warmia and Mazury in Olsztyn  
ul. Oczapowskiego 11, 10-957 Olsztyn, Poland  
E-mail: wojciech.sobieski@uwm.edu.pl

**Abstract.** We propose an algorithm for upscaling of flow with inertia within a multiscale framework ranging from porescale (microscale) to lab scale (mesoscale). In particular, we solve Navier-Stokes equations over complex pore geometries and average their solutions to get flow parameters at mesoscale. For periodic geometries, this is exactly the idea of homogenization. As concerns averaging, we follow the methodology derived in our previous work, which was succesful in deriving stable parameters for flow with inertia, i.e., Forchheimer flow model, at mesoscale. The focus of this paper is twofold: i) to verify that results of our computational experiments are stable in the homogenization limit, and ii) to compare those virtual results with those from physical experiments.

# 1 Introduction

In many mathematical models of important phenomena with real-life applications, one faces the challenge of multiple spatial and temporal scales. This is true in particular in the study of flow and transport in porous media, which is important in environmental studies, geophysics, reservoir engineering, chemical engineering, and medicine.

The multi-scale nature of porous media is well known. In this work we are going to deal mainly with microscale, also referred to as porescale, and with lab-scale, also called mesoscale or Darcy scale. At microscale, a porous medium is represented as a rigid solid skeleton with fluid flowing through pores (void space). At mesoscale, it is seen as a continuum: a permeable material. Other scales relevant to porous media include macroscale which is appropriate in large regional groundwater flow models and in oil reservoir engineering. Passage from mesoscale to macroscale is known as *upscaling* and will not be addressed here. See [37, 45, 25] for general overview and references and specifically [22, 29] for results on upscaling Forchheimer flow from mesoscale to macroscale.

In this work following [35, 34] we are interested in flow at micro- and meso-scale. The flow through porous media at microscale is described, in general, by Navier-Stokes equations, and the flow at mesoscale is described by Darcy's law or its extensions.

Darcy's law [6] postulates a linear relationship between pressure drop and flow rate. It has been shown first in [19] that its validity is restricted to a limited range of flow velocities quantified by a Reynolds number  $Re$ . In [19] it is proposed that the inertia effects start to play a significant role for higher values of  $Re$  and a linear law is not valid any more. To account for inertia terms, Forchheimer proposed a quadratic correction term. The coefficient  $\beta$  associated with the correction term is, however, hard to find experimentally and has been the subject of many discussions and controversies; see the discussion in [40]. In fact, there is actually no agreement even as concerns the form of the nonlinear correction. The mathematical theory of homogenization states however that, as long as a certain scaling with a parameter  $\epsilon$  denoting the relative grain size to the size of the domain is applied, one can relate the local averages of porescale computations to some flow model at mesoscale.

These difficulties and ambiguities motivated on one hand our experimental work [40] on flow with inertia and on the other hand the idea of a computational (virtual) laboratory in which we connect the flow at microscale with the averaged flow at mesoscale [35, 34]. The latter idea has not been feasible until recently. However, thanks to a significant increase in computational power in the last decade, numerical solutions of Navier-Stokes equations in pore geometries, i.e. at microscale, can be now obtained not only for one pore, but actually for a domain composed of a considerable number of pores. While our initial work [35] was successful in connecting the porescale to mesoscale, it was clear that the numerical approximation of the solutions to Navier-Stokes equations required care to ensure convergence and stability [34].

The next natural research question is to relate these results to their mathematical foundations and to verify i) whether the ideas of homogenization and, in particular, the scaling of coefficients, can be interpreted using the computational models and, in other words, whether they remain stable with grain diameters going to 0. In addition, we set out to verify ii) how the coefficients obtained in computational experiments compared with

experimental values from our other work on flow with inertia [40]. These two questions are addressed in this paper.

If answers to i) and ii) are affirmative, our computational method can be seen as a prototype of a virtual laboratory which can be used *en lieu* of physical experiments. We describe the steps to verify i) and ii) below.

First we set up the virtual laboratory. We start by defining a reference microscale geometry for the porous medium. We mention several methods which can help to identify porescale geometry including micro-computerized tomography images [8], models of virtual reconstruction of porous samples based on modelling of geological processes of rock formation [28], random structures generation [27], and different variants of regular structures of solid-void space distribution [12, 21, 4]. However, in this paper we restrict ourselves to a periodic geometry appropriate for i). We consider grain diameter of a similar size to those measured in experiments and use the simplest virtual microstructure consisting of equally distributed spheres/circles. The flow is driven by boundary conditions; this is not a standard set-up for homogenization.

Second, given the microscale geometry, we simulate fluid flow through the pores numerically. We use a continuum level method, i.e., we use a numerical discretization of Navier-Stokes equations. These are well studied, but their use in complex geometries requires fine grids and is, in general, nontrivial. In our approach we use a finite-volume discretization [43]. Alternative non-continuum methods include Lattice-Boltzman methods [28] and pore network models [33, 13].

Third, we use averaging to get macroscale values of velocity and pressure drop, and calculate the values of effective coefficient of proportionality called conductivity. This calculation is only superficially straightforward, since the stability of results with respect to grids and algorithms over a large range of Reynolds numbers must be ensured.

The results of these three steps are applied in a series of experiments to periodic geometries of a decreasing value of  $\epsilon$ . Based on these we verify i). Next, to answer ii), we compare the results of the reference case to the experimental data. Details, theoretical framework and discussion are shown below.

To our knowledge, the approach in this work following [35, 34] is the first such result in the literature. Related work in [3, 11, 30, 12] addressed the qualitative character of inertia at porescale without deriving upscaled models, discussing homogenization, or comparison with experimental data.

This paper is organized as follows. In Section 2 we recall mathematical models of flow at micro- and mesoscale. Computational laboratory concepts and averaging techniques are described in Section 3. Section 4 discusses the homogenization aspects of the project, i.e., addresses i). Special attention is paid to the issue of boundary conditions which are driving the flow instead of external forces. In Section 5 we address ii), i.e., we compare experimental data with values computed for the synthetic porous medium. We conclude and outline open questions in Section 6.

## 2 Mathematical models at porescale and macroscale

Let  $\Omega \subset \mathbb{R}^d$ ,  $d = 2, 3$  be an open bounded domain occupied by a porous medium and the fluid within. For simplicity in what follows only  $d = 2$  will be considered. We denote by  $(\mathbf{q})_i$ ,  $i = 1, 2$  the components of a vector  $\mathbf{q} \in \mathbb{R}^2$ , and  $\mathbf{e}_1$  and  $\mathbf{e}_2$  denote unit vectors of a coordinate system.

### 2.1 Flow at porescale

At porescale the solid and liquid phases are distinct. Let  $\Omega_F$  be the part of  $\Omega$  occupied by the fluid and denote the solid by  $\Omega_R$ . Let  $\Gamma = \partial\Omega_F \cap \partial\Omega_R$  be the rock–fluid interface, and denote the external boundary of flow  $\Gamma_{ext} := \partial\Omega_F \cap \partial\Omega$ ; it is composed of the inflow  $\Gamma_{in}$  and outflow  $\Gamma_{out}$  parts. Also, we have  $\partial\Omega_F = \Gamma_{ext} \cup \Gamma$ .

We consider an incompressible Newtonian fluid of velocity  $\mathbf{u}$  and pressure  $p$ , flowing in  $\Omega_F$ . The fluid’s viscosity is denoted by  $\mu$  and the (constant) density by  $\rho$ .

The flow is driven primarily by external boundary conditions, such as in a lab core. We prescribe the inflow velocity at  $\Gamma_{in}$  with maximum denoted by  $u_{in}$  and parabolic shape between the walls. On  $\Gamma_{out}$  we impose a numerical outflow condition [43]. On internal boundaries  $\Gamma$  we assume the *no-slip* condition  $\mathbf{u} = 0$ .

Reynolds number  $Re = \frac{|\mathbf{u}|\delta}{\mu}$ , where  $\delta$  stands for a characteristic length in the domain of the flow, e.g., width of a channel or the diameter of porous grains, is routinely used to distinguish between different flow regimes [44, 24, 26, 40]. In porous media the linear laminar flow regime corresponds to  $Re < 1$ , the nonlinear regime is for  $1 \leq Re < 10$ , and turbulence may occur for  $Re \geq 10$  [39, 6]; the turbulence rarely occurs in porous media. The values of  $Re$  characterizing the flow regimes given above vary depending on a quantitative definition of the end of each regime, on a structure of a medium, and on a definition of the Reynolds number itself [44, 40]. In our computational experiments the value of  $Re$  is related to the inflow velocity  $u_{in}$ .

Now we discuss the mathematical model for flow at microscale (porescale). For steady-state flow, in the absence of forces and mass source/sink terms, the momentum and mass conservation in Eulerian frame are expressed by the Navier-Stokes system [5]. After setting for simplicity in the presentation  $\rho \equiv 1$  and rescaling variables with  $\mu$ , we have the stationary Navier-Stokes equations

$$\nabla \cdot \mathbf{u} = 0, \quad \mathbf{x} \in \Omega_F, \quad (2.1)$$

$$\mathbf{u} \cdot \nabla \mathbf{u} - \mu \Delta \mathbf{u} = -\nabla p, \quad \mathbf{x} \in \Omega_F. \quad (2.2)$$

An alternative formulation in terms of the vorticity vector  $\omega = \nabla \times \mathbf{u}$  and the stream function  $\psi$  defined by  $\mathbf{u} = \nabla \times \psi$  was considered in [35].

For small  $Re$ , viscous effects dominate and the nonlinear convective, i.e., inertia terms associated with  $\mathbf{u} \cdot \nabla \mathbf{u}$  are dropped from (2.2), resulting in the linear Stokes approximation; see Section 4.

## 2.2 Flow at Darcy scale

At Darcy (lab scale/mesoscale) the boundaries between  $\Omega_F$  and  $\Omega_R$  are not recognized. Instead, the average flow in  $\Omega$  characterized by average pressure  $P$  and velocity (flux)  $\mathbf{U}$  is considered. Mass conservation  $\nabla \cdot \mathbf{U} = 0, \mathbf{x} \in \Omega$ . The flow is driven by boundary conditions which average porescale boundary conditions.

Darcy's law is a linear momentum equation at mesoscale

$$\mathbf{K}^{-1}\mathbf{U} = -\nabla P, \quad \mathbf{x} \in \Omega, \quad (2.3)$$

where  $\mathbf{K}$  is the conductivity tensor; its values are measured experimentally [6]. More precisely,  $\mathbf{K}$  may be expressed as  $\mathbf{K} = \frac{\kappa}{\mu}$  with absolute permeability tensor  $\kappa$  reflecting properties of the medium. In what follows, notions of  $\mathbf{K}$  and  $\kappa$  will be used alternatively.

In general,  $\mathbf{K} = \begin{bmatrix} K_{11} & K_{12} \\ K_{21} & K_{22} \end{bmatrix}$  for flow in  $d = 2$  dimensions, and is symmetric. If coordinate axis are aligned with the principal directions of the porous medium, then  $\mathbf{K}$  is diagonal. Furthermore, in isotropic media  $\mathbf{K}$  is diagonal and  $K_{11} = K_{22}$ . Due to large viscous dissipation and interstitial effects common in porous media, Darcy's law is a good approximation for a large class of flow phenomena.

For large flow rates Darcy's law is not accurate. In the nonlinear laminar regime with significant inertia a non-Darcy model which extends (2.3) reads

$$\mathcal{K}^{-1}(\mathbf{U})\mathbf{U} = -\nabla P, \quad \mathbf{x} \in \Omega. \quad (2.4)$$

The Forchheimer model  $\mathcal{K}^{-1}(U) := K^{-1} + \beta|U|$  was first proposed for the scalar case  $\Omega \subset \mathbb{R}$  [19]; it was extended to multidimensional isotropic media [16, 6, 39, 14] and is used in petroleum industry around wells [17] in the form

$$\mathcal{K}^{-1}(\mathbf{U})\mathbf{U} := (\mathbf{K}^{-1} + \beta|\mathbf{U}|)\mathbf{U} = -\nabla P, \quad \mathbf{x} \in \Omega. \quad (2.5)$$

The form of nonlinear map  $\mathcal{K}$  for general anisotropic 2D and 3D media has been the subject of theoretical research [31, 20, 23, 10]. Experimental studies [26, 40] focus on identification of flow regimes. There are controversies and inconsistencies concerning the form of  $\mathcal{K}$  as well as the values of the coefficient  $\beta$ .

## 3 Computational model

Now we recall the set-up of our virtual lab described originally in [35, 34]. The computational lab is restricted in this paper to  $d = 2$ . The case of  $d = 3$  is not substantially harder logically but requires much more pre-processing and computational power. Once all elements of the virtual laboratory are well understood, we will consider 3D geometries.

Our computational laboratory includes two elements: fluid flow simulations at porescale and *upscaling* to mesoscale. We discuss both below.

The aim of *upscaling* is to derive models with effective coefficients at higher scale and to incorporate as many processes and nonhomogeneities from the lower scale as possible. There are two main methodologies for upscaling: homogenization- and volume averaging-based approaches.

The homogenization theory provides theorems on convergence of the averages of lower-scale quantities to the higher scale counterparts together with appropriate formulas [7, 38]. A good control of the error estimates and qualitative analysis is provided. Homogenization is essentially restricted to periodic geometries at lower scales; this may be an important limitation. However, in periodic geometries, the computations may be performed on an elementary cell only. The volume averaging based techniques belong to a second group of methods used in upscaling. There are no restrictions with respect to geometry patterns provided the region of averaging, i.e., REV  $\equiv$  Representative Elementary Volume, is large enough to ensure stability of averaged quantities, and small enough not to be influenced by boundary conditions. Effective parameters are computed based on volume averages of microscale variables. In Section 4 we discuss the homogenization approach and link the volume averaging approach to convergence results provided by homogenization theory.

Now we go over the sequence of steps performed in the computational laboratory. We start by defining the geometry of a synthetic porous medium at microscale and an appropriate grid at mesoscale. The subscript  $h$  is associated with numerical solutions at microscale and  $H$  applies at mesoscale.

A synthetic porous medium is defined by a regular structure of equally distributed circles of equal radii representing solid grains; while  $\Omega_F$  is the space between the grains, see Figure 2. We define an unstructured mesh of triangular elements over  $\Omega_F$ ; the parameter  $h$  is the maximum diameter of the mesh elements. We solve the steady-state Navier-Stokes equations (2.1)–(2.2) numerically and obtain  $\mathbf{u}_h$  and  $p_h$ . The method is based on finite-volume discretization [18, 43]. Mesh generation and computations are performed under ANSYS FLUENT software [18].

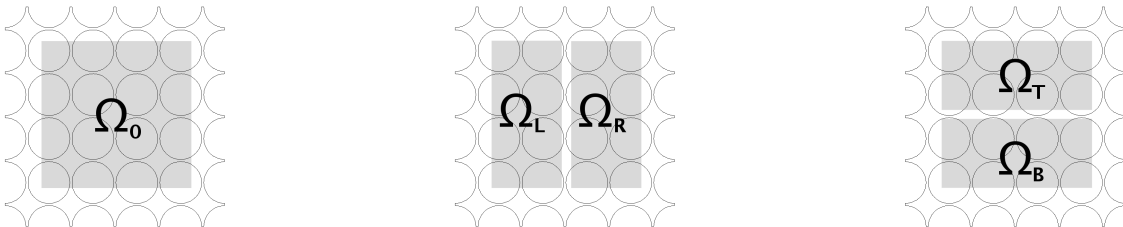


Figure 1: Macrocells used in upscaling

Next we consider mesoscale grid over  $\Omega$ . It is often the case that upscaling is performed with respect to a specific discretization scheme to be implemented at a higher scale. Our approach [35, 34] is inspired by the conservative cell-centered finite difference (CCFD) method and resembles the ideas of mesoscale upscaling in porous media from [15], providing at the same time a bridge to macroscale as in [22]. In CCFD the cell centers are associated with pressure unknowns  $P_H$  and the cell edges are associated with velocity unknowns  $\mathbf{U}_H$ . We impose a similar structure in our averaging approach.

Assume we are concerned with flow in  $\Omega_F$  around some point  $\mathbf{X}_0 \in \Omega_0 \subset \Omega$ . In order to define the averages over  $\Omega_0$ , a mesoscale discretization needs to be superimposed over the microscale grid, see Figure 1. Solving numerically the Navier-Stokes equations (2.1)–(2.2) we obtain  $\mathbf{u}_h, p_h$ . Next we identify the values  $\mathbf{U}_H, P_H|_{\mathbf{x}_0}$  at Darcy scale with some

averages  $\langle \mathbf{u}_h^j \rangle, \langle p_h^j \rangle$  over  $\Omega_0 \subset \Omega$ . The set  $\Omega_0$  is a proper subset of  $\Omega$ , we make sure that the boundaries of  $\Omega_0$  are far enough from inlet and outlet boundaries  $\Gamma_{in}, \Gamma_{out}$  of  $\Omega$  to avoid any numerical boundary artifacts.

Now, in order to compute  $\mathbf{K}$ , a discrete form of (2.3) and of  $\nabla P_H$  is needed. In [15] such values are inferred from boundary conditions. In our case this is not directly possible since the boundary conditions are defined at porescale. Instead, we partition  $\Omega_0$  into pairs of cells,  $\Omega_L, \Omega_R$ , and  $\Omega_T, \Omega_B$ , see Figure 1. The first component of the gradient is calculated as  $G_{LR} = \frac{P_L - P_R}{x_R - x_L}$ , where  $P_L = \langle p_h \rangle_{\Omega_L}$ ,  $P_R = \langle p_h \rangle_{\Omega_R}$ , with  $x_R$  and  $x_P$  denoting  $x$ -coordinates of centers of gravity of  $\Omega_L$  and  $\Omega_R$ . Analogically we get  $G_{BT} = \frac{P_B - P_T}{y_T - y_B}$ . The velocity is computed as  $\mathbf{U}^j = \langle \mathbf{u}_h^j \rangle_{\Omega_0}$  and it has components  $(U_{LR}^j, U_{BT}^j)$ .

In order to find four unknown components of  $\mathbf{K}$  from  $\mathbf{U} = -\mathbf{K}\nabla P$ , we need two independent sets of data for  $\mathbf{U}^j$  and for the associated pressure drops  $G$  so that the system

$$\begin{bmatrix} U_{LR}^1 \\ U_{BT}^1 \\ U_{LR}^2 \\ U_{BT}^2 \end{bmatrix} = \begin{bmatrix} G_{LR}^1 & G_{BT}^1 & & \\ & & G_{LR}^1 & G_{BT}^1 \\ G_{LR}^2 & G_{BT}^2 & & \\ & & G_{LR}^2 & G_{BT}^2 \end{bmatrix} \begin{bmatrix} K_{11} \\ K_{12} \\ K_{21} \\ K_{22} \end{bmatrix} \quad (3.6)$$

has a unique solution.

To generate data  $\mathbf{U}^1, \mathbf{U}^2$  and the associated pressures, we set up virtual flow experiments  $j = 1, 2$  with boundary conditions forcing the flow in different directions for each  $j$ . The easiest is to ensure that the (global) flow directions are essentially orthogonal.

Note that we do not explicitly impose the symmetry  $K_{12} = K_{21}$  which is a fundamental property of the tensor  $\mathbf{K}$ . Rather, we expect it to hold for computational results. A numerically confirmed symmetry is one of the measures of the quality of numerical experiments.

Repeating the experiment described above for increasing values of  $Re$ , we obtain a sequence of corresponding values of  $\mathcal{K}$  in (2.4) and are able to compute  $\beta$  by inverse modeling.

## 4 Homogenization approach

Now we discuss our computational experiments within the homogenization framework in order to address issue i) from the Introduction. We use notation from Section 2 and the traditional notation for Sobolev spaces  $H^k(\Omega)$  [1, 42].

First we discuss Stokes flow which is a linearization of (2.1), (2.2). The flow is driven by external forces appearing in the momentum equation (4.7), and by external boundary conditions (4.9). The mathematical model for Stokes flow is given by

$$\nabla p - \mu \Delta \mathbf{u} = \mathbf{f}, \quad \mathbf{x} \in \Omega_F, \quad (4.7)$$

$$\nabla \cdot \mathbf{u} = 0, \quad \mathbf{x} \in \Omega_F, \quad (4.8)$$

$$\mathbf{u} = \mathbf{g}, \quad \mathbf{x} \in \partial\Omega_F, \quad (4.9)$$

where  $\mathbf{f} \in (H^{-1}(\Omega_F))^d$  and  $\mathbf{g} \in (H^{1/2}(\partial\Omega_F))^d$  are given. We require for well-posedness that the boundary  $\partial\Omega_F$  is  $C^2$  smooth [42]<sup>1</sup>, and that the compatibility condition

$$\int_{\partial\Omega_F} \mathbf{g} \cdot \mathbf{n} = 0 \quad (4.10)$$

is satisfied.

**Remark 4.1** *Based on these conditions it is shown in [42], [Chapter 1, Theorem 2.4], that there exists a unique solution  $(\mathbf{u}, p) \in (H^1(\Omega_F))^d, L^2(\Omega)/\mathbb{R}$  to (4.7), (4.8), (4.9). If  $f, \mathbf{g}$  vanish simultaneously, it follows that  $p \equiv \text{const}, \mathbf{u} \equiv 0$ .*

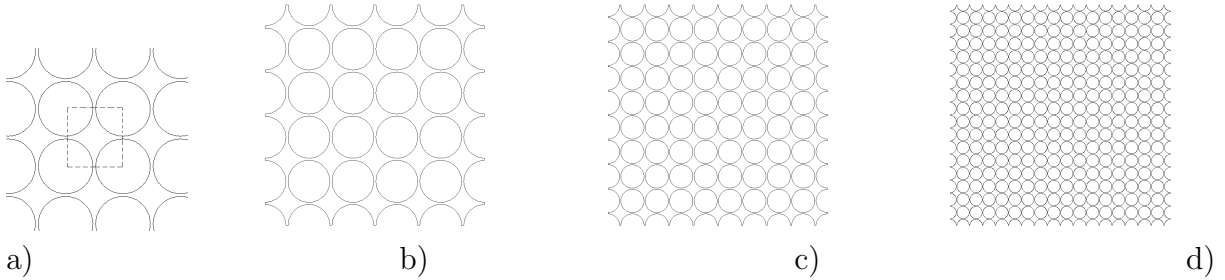


Figure 2: Homogenization approach a) elementary cell, b)  $\Omega_F^{\epsilon_1}$ , c)  $\Omega_F^{\epsilon_2}$ , and d)  $\Omega_F^{\epsilon_3}$

We now give consideration to the terms  $f, \mathbf{g}$  driving the flow.

In the problem of interest to us which is determination of the flow coefficients at lab scale, we envision a computational experiment simulating a physical experiment in a laboratory in which a core is filled by a porous medium and a fluid. The fluid flows due to a pressure difference which can be measured. After the flow rates are measured, the conductivity coefficient is determined as a proportionality constant between the flow rate and pressure drop. It is not necessary in such experiments to consider gravity since the core can be placed horizontally; in this case  $\mathbf{f} \equiv \mathbf{0}, \mathbf{g} \neq \mathbf{0}$ .

As concerns  $\mathbf{g}$ , it needs to be prescribed on  $\partial\Omega_F = \Gamma_{ext} \cup \Gamma = \Gamma_{in} \cup \Gamma_{out} \cup \Gamma$ , and we shall prescribe  $\mathbf{g}$  that is continuous on  $\Gamma_{in} \cup \Gamma$  which then satisfies  $\mathbf{g} \in (H^{1/2}(\partial\Omega_F))^d$ . It is customary to prescribe the no-slip condition  $\mathbf{g}|_{\Gamma} = \mathbf{0}$  on the walls of porous medium  $\partial\Omega_R$ , and from this follows that the condition on  $\Gamma_{ext}$  must honor the compatibility that  $\mathbf{g}|_{\Gamma_{ext} \cap \Gamma} = \mathbf{0}$ . It remains to define  $\mathbf{g}|_{\Gamma_{ext}}$ .

For the inflow condition  $\mathbf{g}|_{\Gamma_{in}}$ , we impose the “usual” parabolic profile between the walls whereby  $\mathbf{g}$  vanishes in contact with the walls  $\partial\Omega_R$ , and achieves maximum in the middle of a pore throat; on straight inflow edges its tangential component is zero. As concerns  $\mathbf{g}|_{\Gamma_{out}}$ , it is important to recall that in numerical experiments one customarily prescribes inflow velocity at  $\Gamma_{in}$  and a numerical outflow condition on  $\Gamma_{out}$  [43], Section 6.2]. This technique avoids numerical instabilities and formation of artificial boundary layers. In other words, we do not prescribe  $\mathbf{g}|_{\Gamma_{out}}$  in numerical experiments.

However, in the discussion below we shall assume that that  $\mathbf{g}$  as a trace of  $\mathbf{u}$  is smooth enough on the entire  $\partial\Omega_F$ . While it is possible to formulate another well-posedness result for the actual problems solved numerically, we will not attempt it.

<sup>1</sup>It is actually shown in [42] that the boundary only has to be Lipschitz.

## 4.1 Homogenization for homogeneous boundary conditions

Now consider the situation in which  $\Omega_F^\epsilon$  has periodic geometry with period size  $\epsilon$ , see Figure 2. It was observed in [38] that the solutions to (4.7)-(4.8)-(4.9) should be periodic, or at least that they should have some periodic components. Additionally, it was postulated that the pressure is close to its local averages and that velocities can be averaged to give an idea of prevailing flow conditions. This “closeness” should become “better” if  $\epsilon$  is smaller. The technique of homogenization then attempts to derive the *effective equations* satisfied by those averages. It turns out that these equations are Darcy’s law (2.3).

In other words, we approximate the solution to a Stokes problem on  $\Omega_F^\epsilon$  by a solution to Darcy problem at lab scale posed in  $\Omega$ . To deal with the fact that fluid/rock boundaries are not recognized at lab scale, one extends the velocities from  $\Omega_F^\epsilon$  to  $\Omega_R^\epsilon$  by zero (they already satisfy a no-slip condition on  $\Gamma$ ); the pressures are extended by their averages; see [2]. One also computes the conductivity coefficient by averaging some auxiliary solutions dependent on pore geometry.

The formal asymptotic expansions and calculations demonstrating that Darcy’s law is effectively an average of Stokes momentum equation, were first shown in [38] and were complemented by a proof of convergence in [41]. The convergence was  $L^2$ -weak for velocities and  $L^2$ -strong for pressures. A stronger result using a corrector was proved by Allaire; see details and references in [[2], Prop.1.2]. The above calculations and convergence proofs are applicable to flow problems driven by an external force field  $\mathbf{f} \neq \mathbf{0}$  and require homogeneous boundary conditions on  $\Gamma_{ext}$ .

In this paper we are interested in discussing  $\mathbf{f} \equiv \mathbf{0}$ , and nonhomogeneous boundary conditions on  $\Gamma_{ext}$ . In what follows we revisit the ideas of homogenization in this context, first considering the case in which  $\mathbf{f} \neq 0, \mathbf{g} \equiv 0$ .

## 4.2 Asymptotics for homogeneous boundary conditions

We briefly recall the ansatz for formal asymptotic expansions in which each variable is expanded in powers of  $\epsilon$ . The usual asymptotic technique is to discern between global and local spatial coordinates  $x$  and  $y = \frac{x}{\epsilon}$ , with  $x \in \Omega, y \in Y$ , where  $Y$  is a unit periodic cell, and to pose equations in which differential operators have components with respect to  $x$  and  $y$  appropriately scaled, e.g.,  $\nabla \mapsto \nabla_x + \frac{1}{\epsilon} \nabla_y$ . Additionally, all components of variables are assumed  $Y$  periodic with respect to  $y \in Y$ :

$$p_\epsilon(x) = p_0(x) + \epsilon p_1(x, y) + \dots, \quad (4.11)$$

$$\mathbf{u}_\epsilon(x) = \mathbf{u}_0(x, y) + \epsilon \mathbf{u}_1(x, y) + \dots \quad (4.12)$$

Next, the idea is to substitute (4.11), (4.12) into (4.7), (4.8) and to match the terms appearing at the same orders of  $\epsilon$ . It is very important [38, 23, 9] to impose the scaling  $\mu = \epsilon^2 \mu_0$  on viscosity, where  $\mu_0$  is some reference value. For simplicity, we set  $\mu_0 \equiv 1$  as in [38].

The calculations lead to an equation satisfied by  $\mathbf{u}_0, p_0$

$$\nabla_x p_0 + \nabla_y p_1 + \Delta_{yy} \mathbf{u}_0 = \mathbf{f}, \quad (4.13)$$

$$\nabla_y \cdot \mathbf{u}_0 = 0. \quad (4.14)$$

If the homogeneous boundary conditions are imposed, then one obtains after averaging (4.14) that  $\nabla_x \cdot \langle \mathbf{u}_0 \rangle = 0$  which is the statement of mass conservation. However, merely averaging (4.13) does not yield momentum equation for  $\mathbf{u}_0$ . Instead, consider multiplying it by a  $Y$ -periodic test function  $\psi \in H^1$ ,  $\nabla \cdot \psi = 0$ ,  $\psi|_\Gamma = 0$ , and integrating over  $Y$ . In this variational formulation of (4.13) one discovers that for any such  $\psi$ ,

$$\int_{Y \cap \Omega_F} (-\mathbf{f} + \nabla_x p_0 + \Delta_{yy} \mathbf{u}_0) \cdot \psi = 0, \quad (4.15)$$

where we have eliminated the second term by integrating by parts and periodicity.

To decouple further, the ansatz  $\mathbf{u}_0 = \sum_i (f_i - \frac{\partial p_0}{\partial x_i}) \omega_i$  conveniently separates scales in (4.13) and (4.15) to yield a local problem to be solved for  $Y$ -periodic  $\omega_i$ , which can be written in the strong form as

$$\nabla_y \pi + \Delta_{yy} \omega_i = \mathbf{e}_i, \quad (4.16)$$

$$\nabla \cdot \omega_i = 0. \quad (4.17)$$

The global mode of variation of  $\mathbf{u}_0$ , or rather its average  $\langle \mathbf{u}_0 \rangle_Y$  over  $Y$ , satisfies

$$\langle \mathbf{u}_0 \rangle_Y = \mathbf{K}(\mathbf{f} - \nabla_x p_0). \quad (4.18)$$

Now, to find  $\mathbf{K}$ , one should first solve the generic problems (4.16)-(4.17) over  $\mathbf{Y}$  for  $i = 1, 2$ , i.e., in at least 2 experiments when  $d = 2$ , and find  $\mathbf{K}$  from its definition

$$(\mathbf{K})_{ij} = (\langle \omega_i \rangle_Y)_j. \quad (4.19)$$

Alternatively, if  $(\mathbf{f} - \nabla_x p_0)$  is known, we could calculate  $\mathbf{K}$  from matching both sides of (4.18). It is clear however that we need two experiments to get  $\mathbf{K}$ . We extend this observation now.

We propose to solve the flow problem (4.7)–(4.9) for  $\mathbf{u}, p$  over a contiguous union  $Y_m$  of  $m$  translations of periodic cells  $Y$  denoted each by  $Y_j$  so that  $Y_m = Y_1 \cup Y_2 \dots \cup Y_m \subset \Omega_F^\epsilon$ . Assuming  $\epsilon$  is small enough and  $m$  not too large with respect to  $diam(\Omega)$ , we can approximate  $\langle p \rangle_{m \times Y} \approx \langle p_0 \rangle_{Y_m}$ ,  $\langle \mathbf{u} \rangle_{Y_m} \approx \langle \mathbf{u}_0 \rangle_{Y_m}$ . Next, since  $p_0$  varies with  $x$ , i.e. with  $j$  indexing  $Y_j$ , we do not have  $\langle p_0 \rangle_{Y_m} \approx \langle p_0 \rangle_{Y_j}$ . However, if  $f$  does not vary too much with  $x$  i.e. within  $Y_m$ , then  $\langle \mathbf{u}_0 \rangle_{Y_m} \approx \langle \mathbf{u}_0 \rangle_{Y_j}$  and  $\langle \mathbf{f} - \nabla_x p_0 \rangle_{Y_m} \approx \langle \mathbf{f} - \nabla_x p_0 \rangle_{Y_j}$  for any  $j$ .

Now the following calculation makes sense. Add (4.18) over all members of  $Y_m$  to obtain

$$\langle \mathbf{u} \rangle_{Y_m} \approx \langle \mathbf{u}_0 \rangle_Y = \mathbf{K} \langle \mathbf{f} - \nabla_x p \rangle_{Y_m}. \quad (4.20)$$

In other words, one can find  $\mathbf{K}$  from matching the two sides of (4.20) for multiple computational experiments. A discussion on how to deal with general anisotropy in  $\mathbf{K}$  is given in [34, 36].

From computational point of view, solving over  $Y_m$  for large  $m$  requires substantial computational power. If that is available, then the approach is more favorable than the use of (4.19) because it generalizes to non-periodic geometries. Most importantly, it has a functional similarity to the one of lab experiments.

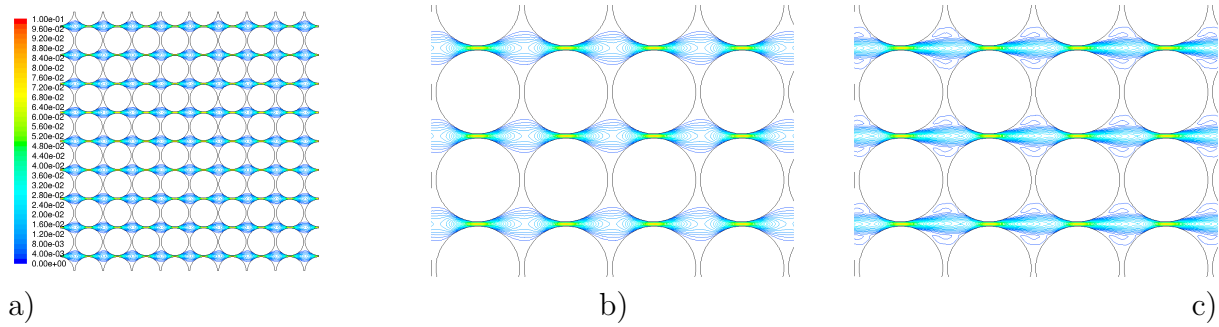


Figure 3: Horizontal flow in  $\Omega_F^\epsilon$ . a)  $u_{in} = 0.1$ , b) zooming-in, c)  $u_{in} = 0.5$ , zooming-in.

The remaining issue is as follows. The Darcy's law (4.18) and the formula (4.19) define  $\mathbf{K}$  regardless whether  $\mathbf{f}$  vanishes or not. However, if  $\mathbf{f} \equiv \mathbf{0}$  and  $\mathbf{g} \equiv \mathbf{0}$ , then by Remark 4.1,  $\langle \mathbf{u} \rangle$  vanishes and  $p_0 \equiv \text{const}$ . While there is no contradiction with (4.18) or (4.20), since both sides of this equation are equal 0, we cannot determine  $\mathbf{K}$  from experiments reflected in (4.18) or (4.20). Therefore, another approach is necessary, in which  $\langle \mathbf{u} \rangle$  does not vanish thanks to nonhomogeneous external boundary condition driving the flow.

### 4.3 Asymptotics for nonhomogeneous boundary conditions

Now we discuss the case when  $\mathbf{f} \equiv \mathbf{0}, \mathbf{g} \neq \mathbf{0}$ .

First let us recall a simple shift from  $\mathbf{g} \neq \mathbf{0}, \mathbf{f} \equiv \mathbf{0}$  to  $\mathbf{g} \equiv \mathbf{0}, \mathbf{f} \neq \mathbf{0}$  as shown in [42]. We decompose  $\mathbf{u} = \mathbf{v} + \tilde{\mathbf{v}}$  so that  $\mathbf{v}, \tilde{\mathbf{v}} \in (H^1(\Omega_F))^d$

$$\nabla \cdot \tilde{\mathbf{v}} = 0, \mathbf{x} \in \Omega_F, \quad (4.21)$$

$$\tilde{\mathbf{v}}|_{\Gamma_{ext}} = \mathbf{g}, \quad (4.22)$$

and we see that

$$\nabla p - \mu \Delta \mathbf{v} = \mu \Delta \tilde{\mathbf{v}}, \mathbf{x} \in \Omega_F, \quad (4.23)$$

$$\nabla \cdot \mathbf{v} = 0, \mathbf{x} \in \Omega_F, \quad (4.24)$$

$$\mathbf{v}|_{\Gamma_{ext}} = \mathbf{0}. \quad (4.25)$$

As a simple example, consider the flow experiment as in Figure 3 where the flow is from left to right and impose a condition so that  $\tilde{\mathbf{v}}(x_1, x_2) = (g_1(x_2), 0)$  where  $g_1$  is any smooth function which vanishes on solid boundaries, for example, represents the parabolic inflow as in Poiseuille flow problem. Note that for such a condition the compatibility condition (4.10) is trivially satisfied, as long as the geometry on the outlet boundary matches exactly the one at the inlet. Also,  $\tilde{\mathbf{v}}$  is divergence free and  $\Delta \tilde{\mathbf{v}} = (g_1''(x_2), 0)$ .

Now consider homogenization in  $\Omega_F^\epsilon$ . First we discuss the behavior of  $\mathbf{u}_\epsilon, \mathbf{v}_\epsilon, \tilde{\mathbf{v}}_\epsilon$  where now, because the geometry of  $\Omega_F$  is periodic, we may consider a boundary condition dependent on both  $x, y$ . Continuing the example as above, set  $\tilde{\mathbf{v}}(x_1, x_2; y_1, y_2) = (g_1(x_2, y_2), 0)$ . As before, the function  $\tilde{\mathbf{v}}$  is divergence free in both  $x$  and  $y$  variables. Furthermore, assume that  $g_1$  is periodic in  $y_2$  and in particular is independent of  $x_2$ . For example, a parabolic profile between the walls can be assumed.

The asymptotic expansions as above now suggest that  $\mathbf{v}_\epsilon$  and  $\tilde{\mathbf{v}}_\epsilon$  may have decompositions similar to  $\mathbf{u}_\epsilon$ , and that, given  $\tilde{\mathbf{v}}_0$ , one could solve the cell-problem for  $\mathbf{v}_0$

$$\nabla_y p_1 + \nabla_x p_0 - \mu \Delta_{yy} \mathbf{v}_0 = \mu \Delta_{yy} \tilde{\mathbf{v}}_0, \quad y \in Y, \quad (4.26)$$

$$\nabla_y \cdot \mathbf{v}_0 = 0, \quad y \in Y, \quad (4.27)$$

$$\mathbf{v}_0|_\Gamma = 0, \quad (4.28)$$

$$\mathbf{v}_0 \text{ periodic in } Y. \quad (4.29)$$

Now notice that  $\tilde{\mathbf{v}}_0$  satisfies  $\nabla_y \cdot \tilde{\mathbf{v}}_0 = 0$ . In addition,  $\tilde{\mathbf{v}}_0$  satisfies the no-slip condition on  $\Gamma$ . In general we cannot guarantee that  $\tilde{\mathbf{v}}_0$  is  $Y$ -periodic. However, in the special case  $\tilde{\mathbf{v}}(x_1, x_2; y_1, y_2) = (g_1(y_2), 0)$  with a  $Y$ -periodic function  $g_1$ , this is satisfied. This means that  $\mathbf{u}_0 = \mathbf{v}_0 + \tilde{\mathbf{v}}_0$  satisfies

$$\nabla_y p_1 + \nabla_x p_0 - \mu \Delta_{yy} \mathbf{u}_0 = 0, \quad y \in Y, \quad (4.30)$$

$$\nabla_y \cdot \mathbf{u}_0 = 0, \quad y \in Y, \quad (4.31)$$

$$\mathbf{u}_0|_\Gamma = 0, \quad (4.32)$$

$$\mathbf{u}_0 \text{ periodic in } Y. \quad (4.33)$$

Averaging as proposed in Section 4.2 we obtain that  $\langle \mathbf{u}_0 \rangle_Y = \langle \mathbf{v}_0 + \tilde{\mathbf{v}}_0 \rangle_Y = -\mathbf{K} \nabla_x p_0$ . An extension to  $Y_m$  and (4.20) is immediate.

We remark that the ansatz proposed here is not the only case in which we obtain an analogue of (4.20). For example, the use of  $\tilde{\mathbf{v}}$  which only depends on  $x$  would also lead to (4.20).

As for the behavior of  $p$ ,  $\mathbf{u}$ , and  $\mathbf{K}$  for large velocities, the Stokes approximation may not be valid and neither is its Darcy average. This is discussed in the next section.

#### 4.4 Homogenization for large velocities

For large velocities, we use (2.2) en lieu of (4.7). It must be appropriately scaled as discussed above:

$$\epsilon^\alpha \mathbf{u}_\epsilon \cdot \nabla \mathbf{u}_\epsilon + \nabla p_\epsilon - \epsilon^2 \mu \Delta \mathbf{u}_\epsilon = \mathbf{f}, \quad \mathbf{x} \in \Omega_F^\epsilon \quad (4.34)$$

This equation is complemented by (4.8) and (4.9) which together make the Navier-Stokes model for flow.

Well-posedness results in [[42], II.1.4 (Theorems 1.5 and 1.6)], while available, depend on the smallness of data  $f, g$ , and on a sufficiently large viscosity  $\mu$ . Additionally, instead of (4.10), we require that  $g = \nabla \times \zeta$  for some smooth function  $\zeta$ .

Upscaling of the Navier-Stokes model to a nonlinear counterpart of (2.3) known as non-Darcy model, has been considered in [38], and [23] as well as in several other sources, see references in [2]. The main controversy appears to be as regards the form of the upscaled model. Within homogenization theory, the discussion centers around the scaling  $\alpha$  of the advective term in (4.34) and of viscosity term. In particular, [32] suggests to use  $\epsilon^2$  for viscosity which we already included in (4.34). In [[25], Section 3.2.2] additionally  $\alpha = 1$  which guarantees that the nonlinear corrections do not “disappear” in the process of passing to the limit with  $\epsilon \rightarrow 0$ .

Another source of difficulties comes from the boundary conditions. The simple linear shift from nonhomogeneous boundary conditions to nonhomogeneous source term does not work for Navier-Stokes system in which a nonlinear term is present. Nevertheless, we apply the same general ideas as in Sections 4.2,4.3 to compute  $\mathcal{K}$  which now depends on  $\langle \mathbf{u} \rangle_Y$ . Additionally, since the magnitude of  $\langle \mathbf{u} \rangle_Y$  depends on the boundary condition, we consider scaling of  $g$  by  $\epsilon$ . We note that there is a concern that with the scaling of viscosity, its “large enough” magnitude required for well-posedness is not guaranteed even though the scaling via  $\alpha$  partially alleviates it.

## 4.5 Computational experiments

Our considerations will be illustrated with computational results. A synthetic porous medium at microscale is defined as described above, see Figure 2 b). The distance between centres of neighboring circles is  $d = 0.002[m]$  and the grain diameter is  $\delta = 0.0019[m]$ , i.e., the radius of grains is  $0.00095[m]$ .

As fluid parameters we use  $\rho = 998.2[kg/m^3]$  and  $\mu = 0.001003[Pa.s]$ , which are properties of water in standard conditions in a lab. What follows,  $Re$  and  $u_{in}$  imposed as a boundary condition are linked by  $Re = 1890,907u_{in}$ . For example,  $u_{in} = 0.001 \rightsquigarrow Re = 1.89$ . Furthermore, to simulate the homogenization procedure and test whether the computational upscaling is stable, we generate a sequence of computational domains  $\Omega_F^{\epsilon_i}, i = 1, 2, 3$ . The reference geometry  $\Omega_F^{\epsilon_1}$  is as in Figure 2 b). To get from  $\Omega_F^{\epsilon_i}$  to  $\Omega_F^{\epsilon_{i+1}}, i = 1, 2$  we apply a factor  $1/2$  to the radii of circles. Computations are performed in all domains independently and are denoted as cases  $\epsilon_1, \epsilon_2$ , and  $\epsilon_3$ .

According to the remark from Section 4.2 we impose scaling of viscosities with a factor  $\epsilon^2$ . That is, for  $\epsilon_2$  we have  $\mu_2 = 0.00025075[Pa.s]$ , and  $\mu_3 = 0.00006268[Pa.s]$  for  $\epsilon_3$ .

As opposed to the theoretical presentation of previous sections, where different models are applied to describe low and large velocity flows, computations are performed in the same way for the whole sequence of  $u_{in}$  values ranging from  $0.00001$  to  $1$ , thus covering linear and nonlinear flow regimes. In general, more iterations of the numerical solver are needed for larger velocities.

Figure 3 gives plots of velocity magnitude distribution. Patterns of flow differ in each flow regime; Figure 3 c) is an illustration of inertia effects.

Now we discuss the results in the context of the homogenization approach. We have several intuitions that we want to verify and confirm. First, as  $\epsilon \rightarrow 0$ , we expect that the pressures and velocities at microscale converge  $L^2$ -strongly and  $L^2$ -weakly, respectively, to their average  $p_0(x)$  which satisfy Darcy’s law. The convergence of pressures is illustrated in Figure 4; we skip the illustration of velocity convergence, as this would require the computation of a corrector. There is a visible difference in pressure shapes obtained for low velocity value ( $u_{in} = 0.1$ ) and large velocities,  $u_{in} = 0.5$  and  $u_{in} = 1$ . Similar pressure curves have been reported in [21, 12]. Our experiments confirm the stability of computational laboratory in the homogenization limit.

Second, we expect that  $\mathbf{K}$  and  $\mathcal{K}$  can be computed reliably. We use the procedure described in Section 3 to find  $\mathbf{K}$  (or  $\mathcal{K}$ ) for a range of imposed velocities  $u_{in}$  and compare results obtained for cases  $\epsilon_1, \epsilon_2$ , and  $\epsilon_3$ .

As is demonstrated in Figure 5 a),  $\mathbf{K}$  remains essentially constant for a large range of

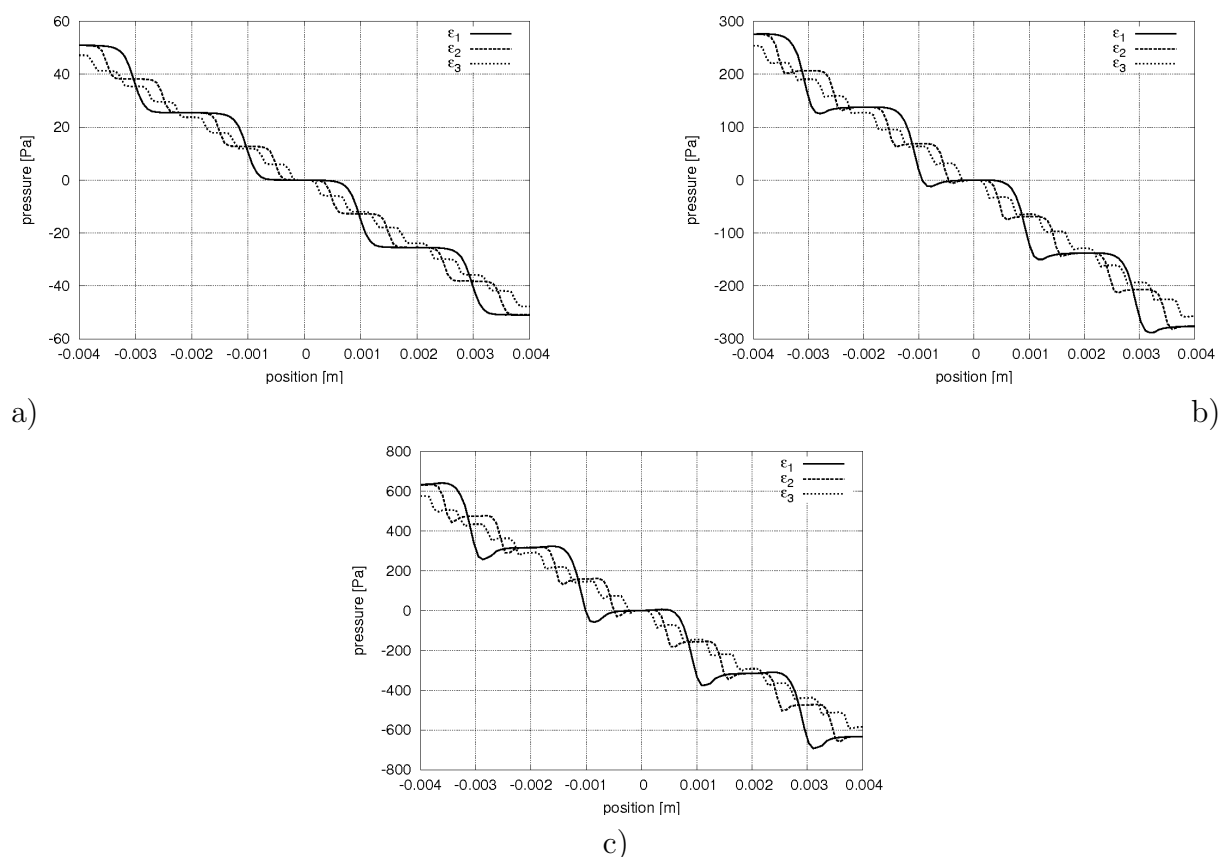


Figure 4: Pressure at  $y = 0$  in  $\Omega_F^{\epsilon_i}$ ,  $i = 1, 2, 3$ . a)  $u_{in} = 0.1$ , b)  $u_{in} = 0.5$ , c)  $u_{in} = 1.0$ .

flow rates, moreover, its values obtained for cases  $\epsilon_1$ ,  $\epsilon_2$  and  $\epsilon_3$  are in a good agreement. Starting from some value of  $u_{in}$  we observe the onset of the nonlinear regime, i.e., that  $\mathcal{K}$  starts decreasing with increasing flow rates as predicted by a nonlinear non-Darcy model (2.4). Equivalently the resistance  $\mathcal{K}^{-1}$  increases with increasing  $Re$ . This qualitative observation is fundamental and is consistent with one in upscaling from mesoscale to macroscale [22]; see also quantitative discussion of  $\mathcal{K}^{-1}$  in [34]. Small differences in the asymptotic behavior of  $\mathbf{K}$  for large velocities are observed.

An interesting result is given in Figure 5 b). We compare  $\mathcal{K}$  computed for the case  $\epsilon_3$  for different scaling schemes applied to  $\mathbf{u}_{in}$  and  $\mu$ . More precisely, we apply 1) scaling  $\mu$  with the factor  $\epsilon^2$  as in Section 4.2, or 2) scaling velocity with a factor  $\epsilon^{1/2}$  and viscosity with the factor  $\epsilon^{3/2}$ , or 3) scaling only viscosity with  $\epsilon^{3/2}$ . For linear regime of flow all the scalings result in the same value of  $\mathbf{K}$ ; still there are differences in  $\mathcal{K}$ . This will be a subject of further studies.

Convergence and stability issues related to the upscaling procedure are not addressed in this work; more results are provided in [34].

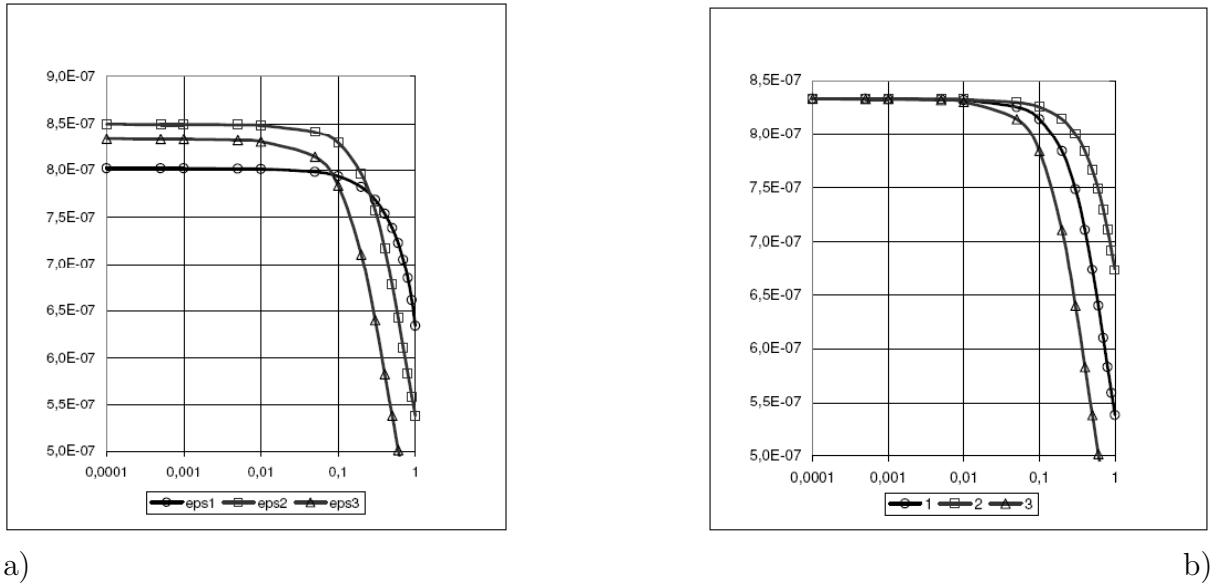


Figure 5: Upscaled permeability a) for  $\Omega_F^i, i = 1, 2, 3$ , no scaling. b) for  $\Omega_F^3$ ; with scaling as follows: 1:  $\epsilon^2\mu$ , 2:  $\epsilon^{3/2}\mu$ ,  $\epsilon^{1/2}u_{in}$ , 3:  $\mu\epsilon^{3/2}$ .

## 5 Physical experiment

To complete our study and address issue ii) from the Introduction, we compare our computational results to the data obtained in the physical experiment reported in [40].

Consider a laboratory stand as given in Figure 6 a). We deal with unconsolidated porous media composed of granulate of diameter  $\delta = 0.00195[mm]$ . During the experiment, 10 independent measurements of water levels are taken for 12 different values of volumetric inflow  $Q^V$ . We calculate mean filtration velocity  $v = Q^V/S$ , where  $S$  denotes the cross-sectional area of a column. The corresponding pressure differences  $p$  between measurements points are computed from water level values. Next we compute absolute permeability  $\kappa$ , following

$$\kappa^{-1}\mu\mathbf{U} = -\nabla P. \quad (5.35)$$

More details about the experiment and values of parameters are given in [40].

Now we compare experimental data to the results delivered by the virtual lab experiment. First we comment on the parameters of synthetic and experimental porous media. We use  $\delta = 0.0019[mm]$  and  $\delta = 0.0018[mm]$  in the former and  $\delta = 0.00195[mm]$  in the latter experiment. These are close but not identical. We expect to find similar but not identical corresponding permeability values.

Next, we discuss scaling between  $\mathbf{K}$  and  $\kappa$  and flow rates. Since our computational experiments delivered  $\mathbf{K}$ , the values of  $\mathbf{K}^{-1}$  in our computational results are multiplied by  $\mu = 0.001003[Pa.s]$  to get  $\kappa^{-1}$ . Additionally, we shift the computational results to fit measured mean filtration velocities by comparing global water inflow. The combined computational and experimental results are shown in Figure 6.

First, we notice the expected qualitative difference between permeabilities computed for  $\delta = 0.0019[mm]$  and those for  $\delta = 0.0018[mm]$ : the conductivities for smaller diameters are larger. Next, we see that the range of velocities covered by the experiment is much smaller than the range of velocities used in computations; this is due to the equipment capacity, more precisely, to the abilities of rotameter of Figure 6 a) acting in a limited range of flow rates. Most importantly, we see a very good qualitative but not perfect quantitative agreement between computational and experimental conductivities. We believe that their closeness is quite satisfactory given that they came from uncorrelated experiments. We also recall the perspective raised in [6] as concerns poor quality of estimated values of  $\kappa$  typically lying between 1/3 and 3 times the true value. These observations address issue ii) raised in Introduction.

In other words, we were able to confirm that the results of the virtual laboratory were within reasonable accuracy with respect to a physical experiment. In addition, the computational lab did not have the limitations of the experimental setup: we could perform experiments in any velocity range insofar as the convergence and stability of the numerical scheme could be ascertained. Moreover, once the preprocessing i.e. the synthetic porescale geometry is completed, it is relatively inexpensive to obtain data for many flow rates while the cost is linear for experimental results.

We consider these results very encouraging. Taking into account all the simplifications made in our virtual model and poor precision of even good laboratory tests, our results compare quite well qualitatively and offer an inexpensive virtual alternative to lab experiments.

## 6 Conclusions

The computational lab can be applied in order to study Darcy's law in the transition from linear to nonlinear flow regime. It may also be used in order to study the nature of the Forchheimer coefficient  $\beta$  and its dependence on various factors, see [35, 34]. We showed that the virtual lab applies to a range of geometries and in particular those suggested by the theory of homogenization. This allows us to find a bridge between elegant mathematical theories of homogenization to a more generally applicable theory of volume averaging.

In addition we showed that the results of the virtual laboratory were within reasonable accuracy with respect to the physical experiment. The benefit of such comparison is multifold. First, the virtual results can be used instead of experimental results. On the other hand, virtual results can be used to guide the set-up of experimental results. Third, once properly calibrated, it could be used to add to the sparse experimental data.

The concept of a computational lab may prove helpful in addressing issues that are hard to handle analytically. More consideration should be given to homogenization for large velocities and to appropriate scaling schemes. A systematic study of permeability behavior as a function of synthetic medium geometry, porosity and other parameters for large ranges of  $Re$  values will be developed in a forthcoming paper.

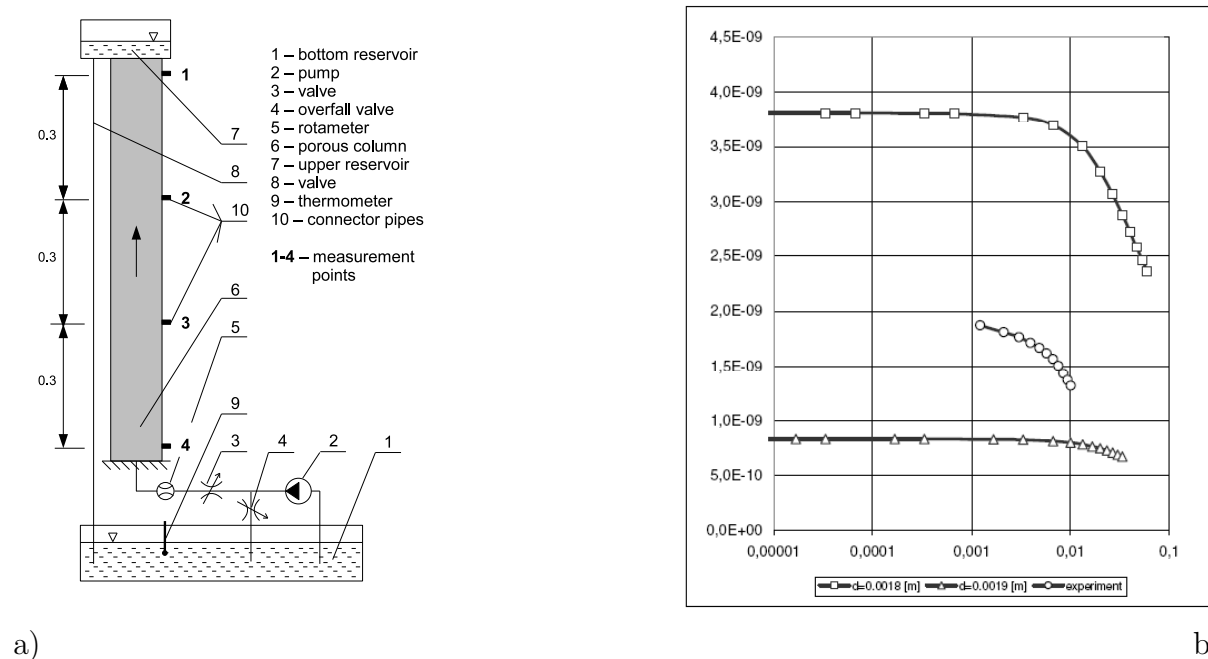


Figure 6: a) Scheme of a laboratory stand: a plexi pipe filled with granulate of diameter  $\delta = 0.00195[\text{mm}]$  (6), recharged from the bottom with water, coming from a container (1) through a pump (2). Intensity of inflow is controlled by a valve (3). After passing through a porous bed, water reaches the upper reservoir (7), and then, through the overfall (8) goes down to the bottom reservoir. The flow intensity is measured by a rotameter (5). Pressures are measured by means of U-tube manometers linked to connector pipes (10). b) Measured and computed permeabilities.

**Acknowledgements:** Peszyńska's research was partially supported from NSF grant 0511190 and DOE grant 98089. We used computational facilities at ICM (Sun Constellation System with AMD Quad-Core Opteron 835X processors) as well as the facilities at Oregon State University including the COE cluster.

## References

- [1] Robert A. Adams. *Sobolev spaces*. Academic Press [A subsidiary of Harcourt Brace Jovanovich, Publishers], New York-London, 1975. Pure and Applied Mathematics, Vol. 65.
- [2] Grégoire Allaire. Mathematical approaches and methods. In Ulrich Hornung, editor, *Homogenization and porous media*, volume 6 of *Interdiscip. Appl. Math.*, pages 225–250, 259–275. Springer, New York, 1997.
- [3] J. S. Andrade, U. M. S. Costa, M. P. Almeida, H. A. Makse, and H. E. Stanley. Inertial effects on fluid flow through disordered porous media. *Phys. Rev. Lett.*, 82(26):5249–5252, Jun 1999.

- [4] B. Bang and D. Lukkassen. Application of homogenization theory related to Stokes flow in porous media. *Applications of Mathematics*, 44:309–319, 1999.
- [5] G. K. Batchelor. *An introduction to fluid dynamics*. Cambridge Mathematical Library. Cambridge University Press, Cambridge, paperback edition, 1999.
- [6] Jacob Bear. *Dynamics of Fluids in Porous Media*. Dover, New York, 1972.
- [7] Alain Bensoussan, Jacques-Louis Lions, and George Papanicolaou. *Asymptotic analysis for periodic structures*, volume 5 of *Studies in Mathematics and its Applications*. North-Holland Publishing Co., Amsterdam, 1978.
- [8] B. Biswal, R.J. Held, V. Khanna, J. Wang, and R. Hilfer. Towards precise prediction of transport properties from synthetic computer tomography of reconstructed porous media. *Physical Review E*, 80:041301, 2009.
- [9] Zhangxin Chen. Expanded mixed finite element methods for linear second-order elliptic problems. I. *RAIRO Modél. Math. Anal. Numér.*, 32(4):479–499, 1998.
- [10] Zhangxin Chen, Stephen L. Lyons, and Guan Qin. Derivation of the Forchheimer law via homogenization. *Transp. Porous Media*, 44(2):325–335, 2001.
- [11] K. J. Cho, M.-U. Kim, and H.D. Shin. Linear stability of two-dimensional steady flow in wavy-walled channels. *Fluid Dynamics Research*, 23:349–370, 1998.
- [12] O. Coulaud, P. Morel, and J.P. Caltagirone. Numerical modelling of nonlinear effects in laminar flow through a porous medium. *J. Fluid. Mech.*, 190:393–407, 1988.
- [13] H. Dong and M.J. Blunt. Pore-network extraction from micro-computerized-tomography images. *Physical Review E*, 80:036307, 2009.
- [14] F.L. Dullien. *Porous media*. Academic Press San Diego, 1979.
- [15] L. J. Durlofsky. Numerical calculation of equivalent grid block permeability tensors for heterogeneous porous media. *Water Resources Research*, 27(5):699–708, 1991.
- [16] S. Ergun. Fluid flow through packed columns. *Chemical Engineering Progress*, 48:89–94, 1952.
- [17] Richard E. Ewing, Raytcho D. Lazarov, Steve L. Lyons, Dimitrios V. Papavassiliou, Joseph Pasciak, and Guan Qin. Numerical well model for non-darcy flow through isotropic porous media. *Comput. Geosci.*, 3(3-4):185–204, 1999.
- [18] Fluent Inc. *Fluent User’s Guide, ver. 6.3*, 2006.
- [19] P. Forchheimer. Wasserbewegung durch Boden. *Zeit. Ver. Deut. Ing.*, (45):1781–1788, 1901.
- [20] M. Fourar, R. Lenormand, M. Karimi-Fard, and R. Horne. Inertia effects in high-rate flow through heterogeneous porous media. *Transport in Porous Media*, 60:353–370(18), September 2005.

- [21] M. Fourar, G. Radilla, R. Lenormand, and C. Moyne. On the non-linear behavior of laminar single-phase flow through two and three-dimensional porous media. *Adv. in Wat. Res.*, 27:669–677, 2004.
- [22] C.R. Garibotti and M. Peszyńska. Upscaling non-Darcy flow. *Transport in Porous Media*, 80:401–430, 2009.
- [23] Tiziana Giorgi. Derivation of Forchheimer law via matched asymptotic expansions. *Transport in Porous Media*, 29:191–206, 1997.
- [24] W. Gray and S. Majid Hassanizadeh. High velocity flow in porous media. *Transport in porous media*, 2:521–531, 1987.
- [25] Ulrich Hornung, editor. *Homogenization and porous media*, volume 6 of *Interdisciplinary Applied Mathematics*. Springer-Verlag, New York, 1997.
- [26] H. Huang and J. Ayoub. Applicability of the Forchheimer equation for non-Darcy flow in porous media. *SPE Journal*, (SPE 102715):112–122, March 2008.
- [27] Y. Jiao, F.H. Stillinger, and S. Torquato. Modeling heterogeneous materials via two-point correlation functions: basic principles. *Physical Review E*, 76:031110, 2007.
- [28] Guodong Jin, T.W. Patzek, and D.B. Silin. Direct prediction of the absolute permeability of unconsolidated and consolidated reservoir rock. *SPE 90084*, 2004.
- [29] M. Karimi-Fard and L.J. Durlofsky. Detailed near-well Darcy-Forchheimer flow modeling and upscaling on unstructured 3d grids. *SPE 118999*, 2009.
- [30] S. Mahmud, A.K.M. Sadrul Islam, and M. A. H. Mamun. Separation characteristics of fluid flow inside two parallel plates with wavy surface. *International Journal of Engineering Science*, 40, 2002.
- [31] C. C. Mei and J.-L. Auriault. The effect of weak inertia on flow through a porous medium. *J. Fluid Mech.*, 222:647–663, 1991.
- [32] Andro Mikelić. Non-Newtonian flow. In Ulrich Hornung, editor, *Homogenization and porous media*, volume 6 of *Interdiscip. Appl. Math.*, pages 77–94, 259–275. Springer, New York, 1997.
- [33] C. Pan, M. Hilpert, and C.T. Miller. Pore-scale modeling of saturated permeabilities in random sphere packings. *Physical Review E.*, 64(066702), 2001.
- [34] M. Peszyńska and A. Trykozko. Convergence and stability in upscaling of flow with inertia from porescale to mesoscale. accepted to *Int. Journal for Multiscale Computational Engineering*, December 2009
- [35] M. Peszyńska, A. Trykozko, and K. Augustson. Computational upscaling of inertia effects from porescale to mesoscale. In G. Allen, J. Nabrzyski, E. Seidel, D. van Albada, J. Dongarra, and P. Soot, editors, *ICCS 2009 Proceedings, LNCS 5544, Part I*, pages 695–704, Berlin-Heidelberg, 2009. Springer-Verlag.

- [36] M. Peszyńska, A. Trykozko, and K. Kennedy. Sensitivity to parameters in non-Darcy flow model from porescale through mesoscale. submitted
- [37] P. Renard, and G. de Marsily. Calculating effective permeability: a review. *Adv. Water Resour*, 20:253–278, 1997.
- [38] Enrique Sánchez-Palencia. *Nonhomogeneous media and vibration theory*, volume 127 of *Lecture Notes in Physics*. Springer-Verlag, Berlin, 1980.
- [39] Adrian E. Scheidegger. *The physics of flow through porous media*. Revised edition. The Macmillan Co., New York, 1960.
- [40] W. Sobieski and A. Trykozko. Darcy and Forchheimer laws in experimental and simulation studies of flow through porous media. in review.
- [41] Luc Tartar. Incompressible fluid flow in a porous medium—convergence of the homogenization process. In *Nonhomogeneous media and vibration theory*, volume 127 of *Lecture Notes in Physics*, pages 368–377. Springer-Verlag, Berlin, 1980.
- [42] Roger Temam. *Navier-Stokes equations*, volume 2 of *Studies in Mathematics and its Applications*. North-Holland Publishing Co., Amsterdam, 1979.
- [43] Pieter Wesseling. *Principles of computational fluid dynamics*, volume 29 of *Springer Series in Computational Mathematics*. Springer-Verlag, Berlin, 2001.
- [44] Z. Zeng and R. Grigg. A criterion for non-darcy flow in porous media. *Transport in Porous Media*, 63:57–69, 2006.
- [45] Wouter Zijl and Anna Trykozko. Numerical homogenization of the absolute permeability using the conformal-nodal and mixed-hybrid finite element method. *Transp. Porous Media*, 44(1):33–62, 2001.